EUROFUSION WPMST1-PR(16) 16124

T Odstrcil et al.

# Optimized tomography methods for high resolution plasma reconstruction at ASDEX Upgrade tokamak

Preprint of Paper to be submitted for publication in
Review of Scientific Instruments

This work has been carried out within the framework of the EUROfusion Consortium and has received funding from the Euratom research and training programme 2014-2018 under grant agreement No 633053. The views and opinions expressed herein do not necessarily reflect those of the European Commission.

# Optimized tomography methods for high resolution plasma reconstruction at ASDEX Upgrade tokamak

T. Odstrčil,[1,2,a)] T. Pütterich,[1] M. Odstrčil,[3] A. Gude,[1] V. Igochine,[1] U. Stroth,[1,2] and ASDEX Upgrade Team[1]
[1)] *Max Planck Institute for Plasma Physics, Boltzmannstr. 2 85748 Garching, Germany*
[2)] *Physik-Department E28, Technische Universität München, Garching, Germany*
[3)] *Optoelectronic Research Center, University of Southampton, Great Britain*

(Dated: June 17, 2016)

The soft X-ray emission provides valuable insight into processes happening inside of the high-temperature plasma. A standard method of deriving the local emissivity profiles of plasma from the line of sight integrals measured by pinhole cameras is the tomographic inversion. Such an inversion is challenging due to its ill-conditioned nature and because the reconstructed profiles depend not only on the quality of the measurements but also on the used inversion algorithm.

This paper provides a detailed description of several tomography algorithms, which solve the inversion problem of Tikhonov regularization with linear computational complexity in number of basis functions. The possibility of combining these methods with Minimum Fisher Information regularization is demonstrated, and various statistical methods for the optimal choice of the regularization parameter are investigated with emphasis on their reliability and robustness. Finally, the accuracy and capability of the method is demonstrated by reconstructions of the experimental SXR profiles, with poloidal asymmetric impurity distribution from the ASDEX Upgrade tokamak.

PACS numbers: 52.25.Vy, 52.25.Xz
Keywords: Plasma, tomography, tokamaks, Tikhonov regularization

## I. INTRODUCTION

High Z materials like tungsten are expected to be an essential part of plasma-facing components (PFC) of the future fusion reactor devices[1–3]. An unavoidable sputtering of these materials caused by plasma wall interaction leads to an influx of the heavy impurities to the plasma. Radiation losses from the partially stripped high Z ions can be beneficiary at the plasma edge because the power exhaust in the divertor is significantly reduced. However, intensive cooling in the plasma core leads to the deterioration of the fusion performance[4]. Moreover, unfavorable impurity transport conditions in the plasma core can be responsible for impurity accumulation and a consequent radiative collapse of the plasma.

The essential tool for monitoring the spatial impurity distribution is the soft X-ray (SXR) radiation. High-Z ions from metal PFC typically dominate the SXR radiation over the low-Z impurities and bulk ions Bremsstrahlung. The local impurity density can be estimated from the known relation between the SXR radiation and impurity density as it is shown in Refs. 4 and 5. The spatial information about the SXR radiation is provided by several pinhole cameras surrounding the plasma. The low number of available lines of sight and sparse coverage of the plasma leads to a non-trivial ill-posed inversion problem of the limited angle tomography[6], i.e. tomography with relatively few cameras.

A large number of various algorithms have been proposed for solving the SXR tomography. Among them, the most common are methods based on series expansion like Cormack-Bessel or Fourier-Bessel[7], maximum entropy methods[8], and Tikhonov regularization based pixel methods[9,10]. However, the very steep dependence of tungsten SXR radiation on the electron temperature along with peaked temperature and tungsten density profiles results in very steep and localized gradients in the SXR radiation. The presence of such features requires a high dynamic range of the tomographic reconstruction (up to 3 orders of magnitude) in order to resolve the radiation profile from the core to the edge, which excludes most of the preceding method. The best results are typically obtained by employing weakly nonlinear algorithms like Minimum Fisher Information (MFI)[9] and Minimum normalized gradient method (MNGR)[11]. A common drawback of the existing algorithms used to solve the pixel methods is cubic computational complexity. The improved algorithms described in this manuscript enable to find a solution to this particular inversion problem with linear complexity in a number of pixel basis functions. Additionally, various methods for a robust and automatic choice of the optimal regularization level are investigated. The performance of the proposed tomographic methods is verified by reconstruction of the SXR emissivity from hundreds of discharges from the ASDEX Upgrade tokamak (AUG).

AUG is a mid-sized tokamak with $R = 1.65\,\mathrm{m}$, $a = 0.5\,\mathrm{m}$, $I_p \leq 1.4\,\mathrm{MA}$, $B_t \leq 3.1\,\mathrm{T}$ equipped with a tungsten covered wall[12]. The metal wall and high heating input power provided by 8 neutral beam injection (NBI) delivering up to 20 MW, 6 MW of ion cyclotron heating and 3.5 MW of electron cyclotron heating make this tokamak well suited for power exhaust studies relevant for

[a)] Electronic mail: todstrci@ipp.mpg.de.

future fusion reactors. The SXR diagnostic is regularly used for the analysis of the impurity transport[13,14], MHD instabilities[15] and poloidal asymmetries of the plasma[16]. All these measurements can benefit from the high-quality tomographic methods described in this article.

The current paper is organized as follows: Section 2 contains a description of the AUG SXR diagnostic, which features a progressive design well suited for the tomography. In Section 3, we give an overview of the tomography problem and Tikhonov regularization method followed by the thorough derivation of the used algorithms in Sec. 4. Various methods for the optimal choice of the regularization level are examined in Section 5. Additionally, since the reconstruction is always subject to experimental errors, a detailed investigation of variance and bias is done in Sec. 6. Finally, the performance of the proposed methods on the real SXR profiles from is AUG presented in Sec. 7.

## II. SXR DIAGNOSTIC ON AUG

The current design of the AUG SXR system is, with a few minor changes, operational since the year 2006[17]. The diagnostic consists of 15 miniature heads assembled to 8 cameras named F,...,M resulting in a total of 208 lines of sight. The cameras H, I and J have three heads; camera K has two and cameras F, G, L and M have only one head due to spatial constraints in the divertor and between the wall tiles. The design of all heads is identical with the focal length of 14.0 mm and the slit of size $0.3\times5.0\,\mathrm{mm}^2$. The arrays of SXR-diodes are centered perpendicularly to the axis of the heads.

Each head is equipped with a linear array of 35 Centronic Series 5T (LD35-5T) diodes of size $4.6\times0.96\,\mathrm{mm}^2$ with $30\,\mu$m separation. The diodes are shielded by circularly curved $75\,\mu$m Be foils attached behind the slits. The measured variability in the filters thickness was below 5 %. The available spectral interval with response higher than 50 % ranges from 2.3 keV to about 13 keV. Roughly only half of the central diodes on a chip are used to limit the range of the incidence angles on their surfaces and the associated variation in their effective thickness and consequently the spectral sensitivity[18,19]. Despite this restriction in the incidence angles, the effective thickness of the diodes can vary by 12 % (Cameras H, J) up to 19 % (camera I) between the central and the edge diodes. The increased effective thickness influences sensitivity only for photons with energies above 7 keV, which usually do not occur at the cold edge plasma, observed by the side channels, therefore this effect was neglected in the calibration.

The positions of all cameras and their observation cones are shown in Fig. 1. Camera F is situated in the tokamak sector 5/16, and the rest is in the sector 11/15 separated by 137°. Because the camera G has almost identical geometry as the camera F+, the toroidal mode number of the emissivity perturbation can be estimated

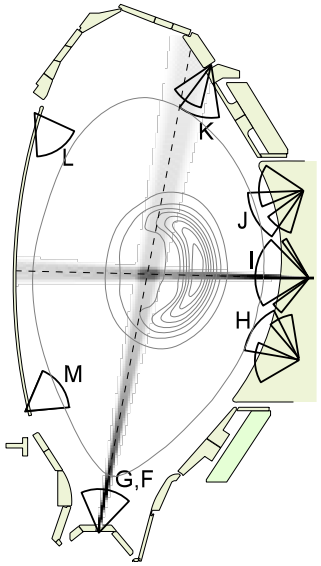


Figure 1. A poloidal projection of the experimental setup of AUG soft X-ray diagnostic system. The viewing cones of each camera are indicated by black circular sectors. Outboard cameras H, I, J and K are composed of multiple heads with the slit in the same position. The viewing geometry of F camera is similar to G, however F is toroidaly separated by 137° from others. In gray are shown the volumes of sights of the core channels for G and I camera and on the background are shown contours of the real SXR emissivity for illustration.

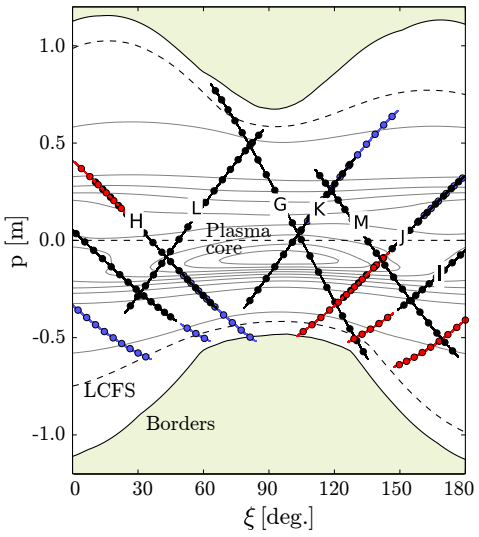


Figure 2. AUG SXR diagnostic (Fig. 1) shown in the projection space, where the LOSs are indicated by the dots in polar coordinates with the pole in the magnetic axis and $p$ and $\xi$ are distance and angle of the LOS tangent. The LOSs of the central heads are colored black, and side heads are red and blue. Contours of the Radon transformation[20] of the radiation profile from the Fig. 1 are shown on the background. Beige area indicates the tokamak vessel. A typical shape of the last closed flux surface (LCFS) is plotted by the dashed line.

merely from the SXR measurements. The location of the cameras also provides almost regular coverage of the projection space[20] shown in Fig. 2 and additionally lines of sight (LOS) from the central head of each camera are always crossing the plasma core. The spatial resolution can be estimated from the width of the volume of sights (VOS) in the plasma core. The full width at half maximum of the vertical VOS of the camera F is 7 cm due to the significant distance from the plasma core but only 4 cm for the horizontal camera I which is the closest. The available spatial resolution of the tomography is moderately improved by synergies of multiple overlapping cameras.

The etendue of the LOSs was calculated by a full 3D model of the VOS including all obstacles in the path[21,22]. Toroidal spreading of the VOS and toroidal curvature of the plasma column cause an outward radial shift of the VOS centroid in the plasma core of around 5 mm compared to the LOS. The largest radial shift is observed for the vertical LOSs of the F,G and K cameras. This effect is included into the tomography by an analytical correction[21].

The signal from the diodes is measured by two distinct acquisition systems. The older one, measuring 80 channels (mainly the H camera and the lower half of the I camera), is equipped with 12-bit analog-digital converters (ADCs) with 500 kHz sampling frequency and an 80 kHz low pass filter. The newer system acquires the rest of the 128 channels with 14 bit ADCs, 2 MHz sampling frequency and a fixed low pass filter at 500 kHz. Both systems are used for the regular tomographic reconstructions and therefore the slower system is interpolated to 2 MHz sampling. The uncertainty of these interpolated channels is slightly increased to reflect the fact that some temporal information was lost. However, only the new system is usable for studying the fast MHD phenomena like toroidal Alfven eigenmodes.

The amplification chain is composed of a preamplifier installed close to the tokamak vessel and a two stage main amplifier in a shielded area. The gain of the preamplifier can be varied in the range 3.75-250 $\mu$A/V and the main amplifier's gain can be set between 1 and $2^{10}$. The power incidenting on the diods is estimated from the general factor 3.62 W/A describing the diods sensitivity in the X-ray range, however an independent absolute calibration was not performed. The gain is adjusted before every experiment for each signal based on the expected emission intensity. The dark current of the diodes is compensated in the main amplifiers before the discharge starts. Additionally, a small offset is add to use the full range of the ADC without cutting off the noise with negative values. After the acquisition, the raw data is stored in a database shotfiles, consuming in total 5.5 GB of disk space per discharge. Finally, because managing of such large data files is very demanding for the memory and computing power, a data edition decimated to 5 kHz is saved as well. It is commonly used for impurity transport and sawtooths studies and observation of slow MHD modes.

## III. PLASMA TOMOGRAPHY

### A. The tomography problem

A pinhole camera does not directly measure the local emissivity but only a signal integrated over the VOS. The goal of the tomography is thus to reveal the best estimate of the local spatial distribution of the emissivity. The power $P_i$ incident on the detector $i$ equals

$$P_i = \iiint_{\mathrm{VOS}} \mathrm{d}\mathbf{r} \frac{\Omega_i(\mathbf{r})}{4\pi} G(\mathbf{r}) \qquad (1)$$

where the integration is done over the whole volume observed by the detector, $\Omega_i(\mathbf{r})$ denotes the solid angle of the cone from the exposed surface of the detector and $G(\mathbf{r})$ is a local plasma emissivity spectrum integrated over the sensitivity range of the detector. The brightness $b_i$ (in units W/m$^2$) can be expressed when both sides of the Eq. (1) are normalized by the *etendue*, defined as a product of the solid angle $\Omega_i$ and area $A$ perpendicular to the axis of the cone $\Omega_i$

$$b_i = P_i \frac{4\pi}{\langle A\Omega \rangle_i} = \iiint_{\mathrm{VOS}} \mathrm{d}l(\mathbf{r}) \eta(\mathbf{r}) G(\mathbf{r}) \qquad (2)$$

where $l$ is the distance between the detector and the point $\mathbf{r}$, $\eta$ is the ratio between the local value of etendue $(A\Omega)(\mathbf{r})$ and average etendue $\langle A\Omega \rangle$ used for the normalization. The set of equations for $b_i$ are the Fredholm integral equations of the first kind which will be solved by discretization on a rectangular grid with the total number of $n$ pixels. Thus, the problem can be rewritten as a set of $m$ linear equations for $m$ detectors

$$b_i = \sum_{j=1}^{n} T_{ij} g_j \qquad i \in 1, \ldots, m \qquad (3)$$

$\mathbf{T} \in \mathbb{R}^{m,n}$ denotes a matrix of the geometry, defining the contribution of a pixel $j$ to the measurement $i$ and $g_j$ is the local emissivity at the $j$-th pixel. The measured brightness $\hat{b}_i$ is subject of usual experimental errors, therefore $\hat{b}_i = b_i + \xi_i$, where $\xi_i$ represents a random error with zero mean and variance $\sigma_i^2$.

### B. Tikhonov regularization

The system of equations obtained by discretization of the Fredholm integral equations is ill-posed and for the tomography of a plasma also usually significantly under-determined ($m \ll n$). A common method to find a unique and sensible solution is the Tikhonov-Philips regularization[23] in the general form which searches for a minimum of a functional $\Lambda(\mathbf{g})$

$$\Lambda(\mathbf{g}) = (\mathbf{Tg} - \hat{\mathbf{b}})^T \mathbf{\Sigma}^{-1} (\mathbf{Tg} - \hat{\mathbf{b}}) + \lambda O(\mathbf{g}) \qquad (4)$$

the first term stands for the data fidelity, i.e. residuum weighted by the expected covariance matrix $\mathbf{\Sigma}$, $O(\mathbf{g})$ denotes a regularization functional and $\lambda$ is a positive regularization parameter balancing the strength of a priori constraints with respect to the goodness of fit. For the sake of simplicity, we will assume further that $\mathbf{T}$ and $\mathbf{b}$ are already weighted by a covariance matrix

$$\mathbf{T} \leftarrow \mathbf{\Sigma}^{-\frac{1}{2}}\mathbf{T} \qquad \mathbf{b} \leftarrow \mathbf{\Sigma}^{-\frac{1}{2}}\mathbf{b}.$$

The purpose of $O(\mathbf{g})$ is to impose a priori knowledge about the emissivity profiles, often some kind of a roughness penalty and a boundary constraint. The regularization operator is typically a quadratic form $O(\mathbf{g}) = \mathbf{g}^T\mathbf{H}(\mathbf{g})\mathbf{g}$, with symmetric and positive semi-definite operator $\mathbf{H} \in \mathbb{R}^{n,n}$ which can be a function of $\mathbf{g}$. The regularization operator therefore includes soft constraints for the solutions. Hard constraints can be imposed by introducing an orthonormal matrix $\mathbf{P} \in \mathbb{R}^{m,l}$ and performing the transformation $\hat{\mathbf{T}} = \mathbf{TP}$, $\hat{\mathbf{H}} = \mathbf{P}^T\mathbf{HP}$ and $\hat{\mathbf{g}} = \mathbf{P}^T\mathbf{g}$. The solution will be restricted to a linear subspace generated by columns of $\mathbf{P}$. An example of $\mathbf{P}$ are the orthonormalized Fourier-Bessel basis functions in the straight field line coordinates.

The solution of the quadratic optimization problem (4) for a constant matrix $\mathbf{H}$ is given by

$$\mathbf{g} = (\mathbf{T}^T\mathbf{T} + \lambda\mathbf{H})^{-1}\mathbf{T}^T\tilde{\mathbf{b}}. \tag{5}$$

Direct inversion of this equation is possible, nevertheless due to large matrices dimension $n$, high computation complexity $\mathcal{O}(n^3)$ and required number of inversion to find proper $\lambda$ this procedure is highly impractical.

The optimization problem (5) has the unique solution if $\ker\mathbf{T} \cap \ker\mathbf{H} = \mathbf{0}$. But, in order to employ computationally efficient numerical algorithms, we will strengthen our assumptions and a regular $\mathbf{H}$ matrix will be required. Regularity can always be imposed by a proper definition of boundary constraints or by adding an identity matrix $\varepsilon\mathbf{I}$ to $\mathbf{H}$, where $\varepsilon$ has the size of the order of the smallest nonzero eigenvalues of $\mathbf{H}$.

### C. Minimum Fisher Information

Among the most common regularization operators belongs an identity operator, suppressing the Euclidean norm of the solution and the Laplace operator reducing the curvature of the emissivity profile[24,25]. Nevertheless, the special features of the SXR profiles, like the peaked distribution of the SXR radiation, the sharp gradients and the large dynamic range, make the nonlinear Minimum Fisher Information regularization (MFI)[9] an ideal candidate for the regularization functional. This functional can be expressed in the following form

$$O_{\mathrm{MFI}}(G) = \iint \mathrm{d}S \frac{1}{G}(\nabla_{\mathbf{u}}G)^T\mathbf{J}_2(\nabla_{\mathbf{v}}G), \tag{6}$$

where $\mathbf{u}(x,y)$ and $\mathbf{v}(x,y)$ are two locally orthogonal vector fields and $\mathbf{J}_2 \in \mathbb{R}^{2,2}$ stands for a matrix of ones. In the case of $\mathbf{u}$ parallel with the Cartesian coordinates, it is called *isotropic* MFI and if $\mathbf{u}$ is locally tangential to the magnetic flux surfaces, *anisotropic* MFI regularization is obtained. More details about the implementation of the anisotropic MFI can be found in Ref. 26. The regularization operator $\mathbf{H}$, representing a linearized and discretized functional (6), takes the form

$$\mathbf{H}^{(k)} = \sum_{\ell\in\{\mathbf{u},\mathbf{v}\}} \mathbf{B}_\ell^T\mathbf{W}^{(k)}\mathbf{B}_\ell, \tag{7}$$

where $\mathbf{B}_\ell$ denotes a discretized gradient operator $\nabla_\ell$ and $\mathbf{W}_{ij}^{(k)}$ is a weight matrix defined as inverse of $\mathbf{g}^{(k)}$

$$W_{ij}^{(k+1)} = \delta_{ij}/\max\{g_j^{(k)}, \varepsilon\}.$$

The Tikhonov regularization must be solved iteratively, because the weight matrix $W$ depends on the emissivity $\mathbf{g}$. The small positive constant $\varepsilon$ prevents zero division and moreover it serves as a positivity constraint. For this work $10^{-8}$ of the emissivity maxima was used, which is usually an adequate compromise between the positivity and a numerical instability caused by too low value of $\epsilon$.

## IV. SPARSE DIAGONALIZATION METHODS

A large variety of methods were developed to solve the Tikhonov problem, for instance the generalized eigenvalues (GEV)[27,28], the singular value decomposition (SVD) method[29], the generalized SVD (GSVD)[25,30], bidiagonalization[31] and the most common is the direct inversion[9,26,32,33]. However, none of these methods in the current implementation is able to take efficiently advantage of all the aspects specific to the Tikhonov regularized SXR tomography. First of all, the projection matrix $\mathbf{T}$ has a small numerical rank $r \leq m \ll n$, while the regularization operator $\mathbf{H}$ is a full rank positive definite matrix. Additionally, both matrices are sparse. The $\mathbf{T}$ matrix for the AUG SXR system has roughly 5 % nonzero elements and the matrix $\mathbf{H}$ has a regular sparsity pattern and approximately 0.01 % fill-in.

In this section, we present modifications of the SVD and QR algorithms for the solution of the Tikhonov regularization that allows taking full advantage of these conditions.

### A. Sparse SVD decomposition (sSVD)

Singular value decomposition is a common tool for the solution of the Tikhonov regularization in the standard form, i.e. when the regularization operator is an identity matrix $\mathbf{I}_n$[34]. Therefore, it is necessary to transform Eq. (5) into the standard form, before the SVD method can be applied. In the case when $\mathbf{H} = \mathbf{L}^T\mathbf{L}$ and $\mathbf{L}$ is invertible, the transformation is straightforward:

$$\bar{\mathbf{T}} = \mathbf{TL}^{-1} \qquad \bar{\mathbf{g}} = \mathbf{Lg}$$

and then by the application of the substitution we get

$$\|\mathbf{T}\mathbf{g}-\mathbf{b}\|_2^2+\lambda\|\mathbf{L}\mathbf{g}\|_2^2=\|\bar{\mathbf{T}}\bar{\mathbf{g}}-\mathbf{b}\|_2^2+\lambda\|\bar{\mathbf{g}}\|_2^2,$$

where $\|\cdot\|_2^2$ denotes the Euclidean norm. This transformation method was proposed by Tarasaki[29] for the Laplace operator. Let's consider a more general case of a sparse and positive definite but otherwise arbitrary matrix $\mathbf{H}$. The transformation to the standard form can be performed very effectively by the sparse Cholesky decomposition[35] of $\mathbf{H}$. A regularized solution is found in the following steps:

1. The sparse Cholesky decomposition of the matrix $\mathbf{H}$ is evaluated through

$$\mathbf{P}\mathbf{H}\mathbf{P}^T=\mathbf{L}\mathbf{L}^T \tag{8}$$

   where $\mathbf{L}$ is a sparse lower triangular matrix and $\mathbf{P}$ is a fill-reducing permutation.

2. In the next step, Eq. (5) is transformed into the standard form

$$\left(\mathbf{T}^T\mathbf{T}+\lambda\mathbf{P}^T\mathbf{L}\mathbf{L}^T\mathbf{P}\right)^{-1}\mathbf{T}^T=\mathbf{P}^T\mathbf{L}^{-T}\left(\mathbf{A}^T\mathbf{A}+\lambda\mathbf{I}_n\right)\mathbf{A}^T \tag{9}$$

   defining the integrated projection matrix $\mathbf{L}^{-1}\mathbf{P}\mathbf{T}^T$ as $\mathbf{A}$. Exploiting the sparsity of $\mathbf{H}$ and $\mathbf{T}$ matrices, such inversion can be evaluated with $\mathcal{O}(nm)$ complexity. The matrix $\mathbf{A}$ is not sparse anymore, except of the empty rows corresponding to the pixels outside of the plasma boundary. For this reason, the SVD in the following step will be evaluated for nonzero rows only.

3. Now, when the standard form is obtained, the solution can be found by the SVD decomposition of the matrix $\mathbf{A}$, i.e. $\mathbf{A}=\mathbf{U}\mathbf{D}\mathbf{V}^T$. Columns of the matrices $\mathbf{U}\in\mathbb{R}^{m,r}$ and $\mathbf{V}\in\mathbb{R}^{n,r}$ are left-singular resp. right-singular vectors of $\mathbf{A}$ and $\mathbf{D}\in\mathbb{R}^{k,k}$ is a matrix with singular values on the diagonal in descending order. Substituting the SVD of $\mathbf{A}$ to Eq. (9) results in a decomposition of a form that is already appropriate for the numerical solution

$$\mathbf{P}^T\mathbf{L}^{-T}\left(\mathbf{A}^T\mathbf{A}+\lambda\mathbf{I}_n\right)\mathbf{A}^T=\tilde{\mathbf{V}}(\mathbf{D}^2+\lambda\mathbf{I}_r)^{-1}\mathbf{D}\mathbf{U}^T$$

   where matrix $\tilde{\mathbf{V}}\in\mathbb{R}^{n,r}$ of the reconstructions basis is defined as $\tilde{\mathbf{V}}\equiv\mathbf{P}^T\mathbf{L}^{-T}\mathbf{V}$. Nevertheless, the matrix $\mathbf{A}$ is "tall-and-slim" and therefore it is more economical to calculate a eigen-decomposition of the smaller Hermitian matrix $\mathbf{A}\mathbf{A}^T$ instead of proper SVD of $\mathbf{A}$.

4. The regularized solution $\mathbf{g}_\lambda$ is obtained in the form of a series expansion

$$\mathbf{g}_\lambda=\sum_{i=1}^{r}f_{i,\lambda}\frac{(\mathbf{U}_i^T\mathbf{b})}{D_i}\tilde{\mathbf{V}}_i. \tag{10}$$

   Here $\mathbf{U}_i$ and $\tilde{\mathbf{V}}_i$ denotes columns of matrices $\mathbf{U}$ and $\tilde{\mathbf{V}}$, respectively. The filtering factors are defined as $f_{i,\lambda}=(1+\lambda/D_i^2)^{-1}$, monotonously decreasing with $\lambda$ and $i$.

The first step, when the Cholesky decomposition of the $\mathbf{H}$ matrix is performed, shows linear complexity because of the regular sparsity pattern and the small number of nonzero elements proportional to $n$. The time spent in this step is negligible. The second step is done by back-substitution of the sparse lower triangular matrix $\mathbf{L}$ with $\mathcal{O}(nm)$ complexity. When SVD is replaced by the eigenvector decomposition (EV), then the required number of operations is scaling as $\mathcal{O}(m^3+nm^2)$ while if the SVD is applied, the number of flops will increase to $2nm^2+11\,m^3$ as it was shown in Ref. 36, and the measured computing time was increased five times. The other steps are also not affecting the final linear complexity. Moreover, our analysis indicates a cubic dependence of the decomposition time on the number of detectors $m$ in the EV.

### B. Sparse QR decomposition (sQR)

An alternative method based on a triple application of the QR decomposition was proposed in Ref. 37 by Hosoda. This method does not provide an accurate solution of Eq. (5), however, the solution is a very close approximation, the difference is usually lower than 0.1 %. Previous comparisons of the original algorithms[29] have shown ten times lower computation cost than the former SVD method.

The description of the optimized algorithm for the decomposition of the sparse matrices is summarized below:

1. The first step is identical to the sSVD method; the matrix $\mathbf{A}$ is obtained via the integration of the projection matrix.

2. In the next step, the pivoted rank-revealing QR decomposition is applied on $\mathbf{A}$

$$\mathbf{Q}_1\hat{\mathbf{D}}\mathbf{S}\overset{RRQR}{=}\mathbf{A}\mathbf{\Pi}, \tag{11}$$

   where $\mathbf{Q}_1\in\mathbb{R}^{n,k}$ is a unitary matrix, $\hat{\mathbf{D}}\in\mathbb{R}^{k,k}$ is a diagonal matrix with positive diagonal values sorted in non-increasing order, $\mathbf{S}$ is an upper triangular matrix with a unitary diagonal and $\mathbf{\Pi}$ is a permutation matrix. The Q-less QR decomposition can be employed, because $\mathbf{Q}_1$ is not required explicitly in the following steps.

3. The ordinary QR decomposition is applied to the matrix $\mathbf{\Pi}\mathbf{S}^T$

$$\mathbf{Q}_2\mathbf{R}_2\overset{QR}{=}\mathbf{\Pi}\mathbf{S}^T$$

   where $\mathbf{R}_2\in\mathbb{R}^{r,r}$ is an upper triangular matrix and $\mathbf{Q}_2\in\mathbb{R}^{m,r}$ is a unitary matrix.

4. Now the diagonal matrix $\mathbf{D}$ is swapped with the $\mathbf{R_2}$ matrix

$$\mathbf{M} = \hat{\mathbf{D}} R_2^T \hat{\mathbf{D}}^{-1}$$

and the third QR decomposition of the matrix $M$ is computed

$$\mathbf{R}_3\mathbf{D}_R\mathbf{Q}_3 \overset{QR}{=} \mathbf{M}$$

as well as in the second step, the Q-less QR decomposition can be used. $\mathbf{R}_3 \in \mathbb{R}^{r,r}$ is an upper triangular matrix with a unitary diagonal and $\mathbf{D}_R \in \mathbb{R}^{r,r}$ is a diagonal matrix.

5. In the last step, the final integration by the $\mathbf{L}$ operator is performed and the decomposition is transformed to the form analogous to the preceding methods

$$\begin{aligned}
\mathbf{R} &= \hat{\mathbf{D}}\mathbf{R}_3^T(\mathbf{D}\mathbf{D}_R)^{-1} \\
\mathbf{D} &= \hat{\mathbf{D}}\mathbf{D}_R \\
\mathbf{U} &= \left(\mathbf{R}_3^{-1}\mathbf{Q}_2^T\right)^T \quad \text{(Forward-substitution)} \\
\mathbf{V} &= \mathbf{A}\mathbf{U}\mathbf{D}^{-1} \\
\hat{\mathbf{V}} &= (\mathbf{P}\mathbf{L}^{-T}\mathbf{V})^T \quad \text{(Back-substitution).}
\end{aligned}$$

Since the definition of the matrices $\mathbf{U}$, $\mathbf{D}$ and $\hat{\mathbf{V}}$ is now consistent with the notation in sSVD algorithms, the regularized solution can be estimated by the formula (10). The arguments used for the analysis of the computaional complexity of the sSVD method are valid here as well. In the sQR algorithm the most expensive step is the first RRQR decomposition requiring $\mathcal{O}(nm^2+m^3)$ operations. The other steps have a $\mathcal{O}(nm)$ complexity or even lower. Since the asymptotic complexity are both algorithms, sSVD and sQR, identical, it is necessary to assess these algorithms by a direct comparison of the computation time.

### C. Computational effort

Additionally to the algorithms introduced in the previous section, also the GEV method[27] based on the GEV routine for sparse Hermitian matrices from the ARPACK library[38] and GSVD[30] were included in the investigation in this section, because both are regularly used for the solution of the generalized Tikhonov problem. The mutual comparison was performed for a variable number of pixels $n$ and with a fixed number of $m = k = 200$ detectors. The number of the nonzero elements in the projection matrix was about 5 % and the used anisotropic regularization operator had all nonzero elements regularly aligned in nine diagonals. All computation tests were run in a single thread on an Intel Core i5-2540M processor to allow a fair comparison of these methods. An algorithm based on the direct inversion of the Tikhonov problem by the sparse Cholesky solver[26] was used a reference method. The measured computation time is shown in Fig. 3 with dashed lines indicating the asymptotic complexity.

The fastest method is based on the sQR decomposition, and it takes about 34 ms for a moderate resolution 40×60 pixels. sQR is followed by the sSVD algorithm that is 30 % slower. Both algorithms are showing a linear time complexity in a number of pixels $n$, which tails off for $n \lesssim 5m$. Other algorithms based on the GEV and the GSVD are for a reasonable range of $n$ significantly slower than the direct inversion. The time measured for the algorithm based on the sparse GEV are indicating a quadratic complexity in $n$ but with rather a large multiplication factor. Moreover, GSVD based on sine-cosine decomposition[39] is not able to efficiently take advantage of the matrix sparsity and, thus the computing time is scaling as $\mathcal{O}(n^3)$.

The decomposition methods even further outperform the direct solvers because at least $3-10$ inversions are necessary to solve the inner loop of the MFI algorithm and find the optimal regularization parameter. On the contrary, once the decomposition is available, the inner loop can be solved instantaneously in $\approx 1$ ms with $\mathcal{O}(mk)$ complexity.

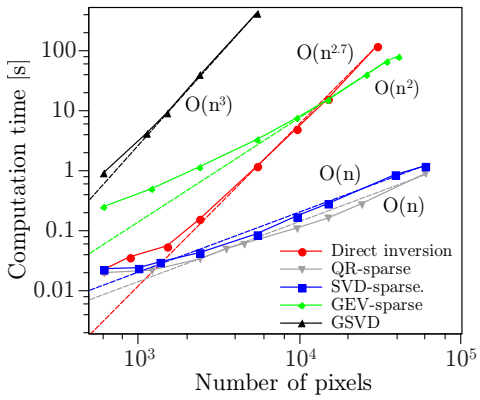


Figure 3. Computation time of different decomposition methods was compared to the direct inversion algorithm based on the sparse Cholesky decomposition[26]. The asymptotic complexity is indicated by the dashed lines.

The sSVD and sQR decomposition methods are very efficient especially in the case of the low-rank projection matrix. The direct inversion is better only in the case of large rank $k$ or very low resolution $n \ll 10^3$ as it was shown in Refs. 40 and 41. If the decomposition is not evaluated for each time frame separately, but instead the discharge is divided into short blocks reconstructed at once, it is possible to compute roughly 200 frames/s at moderate resolution 40×60 px in a single thread.

## V. THE OPTIMAL CHOICE OF THE REGULARIZATION PARAMETER

One of the key issues related to the Tikhonov regularization is the proper selection of the regularization parameter. The optimal parameter $\lambda_{\mathrm{opt}}$ is minimizing the difference between the reconstructed and the original profile. Since the original radiation distribution is not available in the experiment, this parameter must be determined purely from the measurements and a priori knowledge. Moreover, the optimal estimator should be robust, reliable and last, but not least, the computation complexity should be polynomial in $m$, independent of the number of pixels $n$. Hence, the optimal solution must be found without the explicit evaluation of the $\mathbf{g}_\lambda$.

Many different methods have been proposed for the choice of the regularization level. Commonly used are the Morozov's discrepancy principle (DP)[6,42], the curvature of the L-curve[43], the generalized cross-validation (GCV)[24,29],the predicted sum of squares (PRESS)[44], the corrected Akaike information criterion ($\mathrm{AIC_C}$)[45] and the quasi-optimality criterion[46,47]. However, except DP, these methods are not commonly used in SXR tomography. Since the behavior of these methods significantly depends on the investigated problem, the only way to identify the most suitable one is to perform a comparison on artificial and experimental measurements. Tests of these methods on the artificial radiation profiles have identified the most promising methods – PRESS, $\mathrm{AIC_C}$, GCV, and DP. Due to the highly ill-posed character of SXR tomography, the corner of the L-curve is insignificant or missing on real measurements. The quasi-optimality criterion is not able to provide a single, reliable and unique optimum even for simple artificial profiles. Additionally, the compatibility to nonlinear MFI needs to be investigated.

The *regularization level* in the following section will be quantified by a quantile $q_\lambda$ in set $\{D_i^2\}$ equal to $\lambda$. Compared to the regularization coefficient $\lambda$ itself, whose value does not have a direct meaning and depends on the normalization of the $\mathbf{H}$ and $\mathbf{T}$ matrices, $q_\lambda$ roughly corresponds to the fraction of degrees of freedom removed by the regularization. A value close to one results in very high regularization, almost completely ignoring the measurements while the value about zero causes negligible regularization.

### A. Discrepancy principle

Morozov's discrepancy principle (DP) is the most common method among the plasma physicists[10,26,33,40,42] for the choice of the optimal regularization parameter. The regularization parameter is chosen such that the residual norm for the solution $\mathbf{g}_\lambda$ satisfies

$$\|\mathbf{T}\mathbf{g}_\lambda - \mathbf{b}\|_2^2 - \|\boldsymbol{\epsilon}\|_2^2 = 0 \qquad (12)$$

where $\boldsymbol{\epsilon}$ is the estimated level of the noise level. This condition together with the minimizing of the regularization functional leads to a constrained quadratic optimization problem, easily solvable by an iterative root-solver. A unique solution satisfying the condition (12) exists if $\|\mathbf{b} - \mathbf{U}\mathbf{U}^T\mathbf{b}\|_2 < \|\boldsymbol{\epsilon}\|_2^2$ and $\|\mathbf{b}\|_2^2 > \|\boldsymbol{\epsilon}\|_2^2$, which is fulfilled always if the projection matrix $\mathbf{T}$ has a full rank and the measurement exceeds the noise level. For the decomposition methods introduced earlier, the residuum can be expressed in the following form

$$\|\mathbf{T}\mathbf{g}_\lambda - \mathbf{b}\|_2^2 = \sum_{i=1}^{m} \left((1 - f_{i,\lambda})\mathbf{U}_i^T\mathbf{b}\right)^2, \qquad (13)$$

where $f_{i,\lambda}$ are filtering factors introduced in Eq. (10), $f_{i,\lambda} = 0$ for $i \geq r$ and $\mathbf{U}$ must be multiplied by the matrix $\mathbf{R}$ from the right for the QR method. The root in $\lambda$ can be found with mere $\mathcal{O}(mk)$ complexity. The choice of Eq. (12) was motivated by the fact, that if the Tikhonov regularization is correctly weighted by the statistical uncertainties and approximately normal noise distribution can be assumed, the residuum will have the $\chi^2$ distribution with $p$ degrees of freedom. The expected value of $\chi^2$ is also $p$ and it can be easily checked that $p = m - k + \sum_{i=1}^{k}(1 - f_i)^2$. Since the existence of the root would not be generally guaranteed, we will assume $p \equiv m$, which leads to Eq. (12) and tends to slightly overestimate the regularization parameter.

The discrepancy principle strongly depends on a reliable estimate of the uncertainty level for each channel and time frame and such knowledge is usually not directly available. We have estimated the statistical variance from the temporal/spatial characteristics of the measured signals. However, the systematic errors are unknown, and they can also depend on the profile or energy spectrum of the radiation. For this reason, different methods depending solely on the measured data must be considered as well.

### B. PRESS - Predicted residual error sum of squares

Predicted residual error sum of squares (PRESS)[48] is based on the leave-one-out cross-validation method. The model that minimizes the PRESS score should have the best predictive capability. Over-fitted models tend to fit noisy features in the data, reducing their predictive capability. On the other hand an over-regularized model is not be able to follow real features in the measurements, leading to an increase of the PRESS as well. The value of PRESS can be expressed by the following formula

$$\mathcal{P}(\lambda) = m^{-1} \sum_{l=1}^{m} \left[\left(\mathbf{T}\mathbf{g}_\lambda^{(l)}\right)_l - b_l\right]^2$$

where $\mathbf{g}_\lambda^{(l)}$ is the solution in which the $l$-th detector was removed. A simplified solution was found for the decomposition based methods[49]

$$\mathcal{P}(\lambda) = \frac{1}{m} \sum_{k=1}^{m} \left( \frac{\sum_{j=1}^{r} \sum_{l=1}^{m} (1 - f_j) U_{kj} U_{lj} b_l}{\sum_{j=1}^{r} (1 - f_j) U_{kj}^2} \right)^2 \qquad (14)$$

and the optimum can be found with $\mathcal{O}(mr)$ complexity. The first comparison of the PRESS method and the GCV method, presented by Iwama[44], show superiority of the GCV, because if the *hat matrix*

$$\hat{\mathbf{A}}_\lambda \equiv \mathbf{T}(\mathbf{T}^T\mathbf{T} + \lambda\mathbf{H})^{-1}\mathbf{T}^T \tag{15}$$

is close to diagonal, the PRESS method is not able to provide a reliable estimate due to lack of redundancy in the model. But this is not the case of SXR tomography, where assumption of smoothness and large number of overlapping LOSs guarantee sufficient redundancy.

### C. GCV - Generalized cross-validation

The underlying principle in the generalized cross-validation (GCV) is very similar to the PRESS method. GCV was first introduced by Wahba[50] and further elaborated by Golub[51] for the ridge regression and used for plasma tomography by Iwama[24,52] later. GCV score is defined as

$$\mathcal{G}(\lambda) \equiv \frac{\|(\mathbf{I}_m - \hat{\mathbf{A}}_\lambda)\mathbf{b}\|_2^2}{\mathrm{Tr}(\mathbf{I}_m - \hat{\mathbf{A}}_\lambda)^2}.$$

Using a decomposition (10) we will obtain

$$\mathcal{G}(\lambda) = \frac{\|\mathbf{T}\mathbf{g}_\lambda - \mathbf{b}\|_2^2}{\left(r - \sum_{i=1}^r f_i\right)^2} \tag{16}$$

and the residuum in the numerator is evaluated from Eq. (13). The existence of a global and unique optimum of the GCV curve is not guaranteed. Consequently, we have observed on real measurements that the proper optimum is not the global one but, if it was present at all, it was the local optimum with the highest regularization.

### D. $\mathrm{AIC_C}$ - Corrected Akaike information criterion

An alternative way of selecting the optimal regularization parameter is a negative entropy minimizing principle called the corrected Akaike information criterion ($\mathrm{AIC_C}$), originally proposed by Hurvich in Ref. 45. $\mathrm{AIC_C}$ is a modification of the well known AIC[53] method corrected for finite size samples. $\mathrm{AIC_C}$ is defined by the following formula:

$$\mathcal{A}_c(\lambda) = \|\mathbf{T}\mathbf{g}_\lambda - \mathbf{b}\|_2^2 + m(\ln(2\pi) + 1) + \frac{2(p+1)m}{m-p-2}$$

where $p$ denotes the number of parameters. The effective number of parameters of the Tikhonov regularization is determined as[54] $p = \mathrm{Tr}(\hat{\mathbf{A}}_\lambda) = \sum f_i$. Because $\mathcal{A}_c(\lambda)$ is not homogenous function of the residuum, the position of the minima will depend on the estimated absolute level of the noise. This means that under real experimental conditions a systematic error can be introduced.

### E. Effect of the nonlinear MFI iterations

The convergence and the final solution of the MFI depend among others on the choice of the regularization parameter in the intermediate steps. The decomposition $\{\mathbf{U}^{(\mathbf{i})}, \mathbf{D}^{(\mathbf{i})}, \mathbf{V}^{(\mathbf{i})}\}$, obtained in each iteration by sSVD or sQR method, is better adapted to describe the solution than the previous one. This is illustrated by reconstruction of a rather peaked phantom (artificial profile) in Fig. 4, where the GCV optimal reconstruction is shown in the upper row and the *energy spectrum* of the $i$-th iteration defined as $(\mathbf{U}^{(\mathbf{i})}\mathbf{b})_j^2$ is in the lower row. In the 0-th MFI iteration, equivalent to the 1. order Tikhonov regularization, the energy spectrum is broad, the signal is mixed with the noise and separation of the dimensions dominated by the random variability is possible only for $i > 150$. But, in the first and the second iteration the spectrum is significantly compressed, and the dimensions dominated by the noise can be now clearly separated for $i > 70$.

The effects of the MFI iteration on different regularization selection methods is summarized in Tab. I. The first column contains the regularization level for each iteration described by $q_\lambda$ in and the second column is the relative deviation of the tomogram $\mathbf{g}_\lambda$ from the known phantom $\mathbf{g}$:

$$\delta = \|\mathbf{g}_\lambda - \mathbf{g}\|_2 / \|\mathbf{g}\|_2. \tag{17}$$

Evidently, the optimal regularization level is increasing with each iteration while $\delta$ is decreasing for all methods. At the same time, the optimum for GCV, PRESS, and $\mathrm{AIC_C}$ methods becomes more pronounced and easier to distinguish due to the better signal/noise separation in the energy spectrum (Fig. 4). GCV and PRESS methods provide the best estimate of the regularization level with the final relative deviation $\delta$ just by 1% higher than the optimum. The discrepancy principle and $\mathrm{AIC_C}$ have both selected over-regularized solutions.

Moreover, we have observed that using the formerly introduced methods in the intermediate iteration steps lead to the significant increase in failure rate of the tomography on the real data and slowing of the convergence. Therefore, we have set the regularization to a fixed value $q_\lambda = 75\%$, which is above the typical regularization level in AUG. The optimal regularization is selected only in the last iteration.

### F. Comparison of the regularization methods using artificial data

The common way to assess the performance of a tomography method is to reconstruct phantom profiles. We have prepared a set of phantoms with increasing complexity, changing from simple Gaussian, over peaked and sharply hollow to a complex hollow-peaked profile as it is shown in Fig. 5. The reconstruction was evaluated with

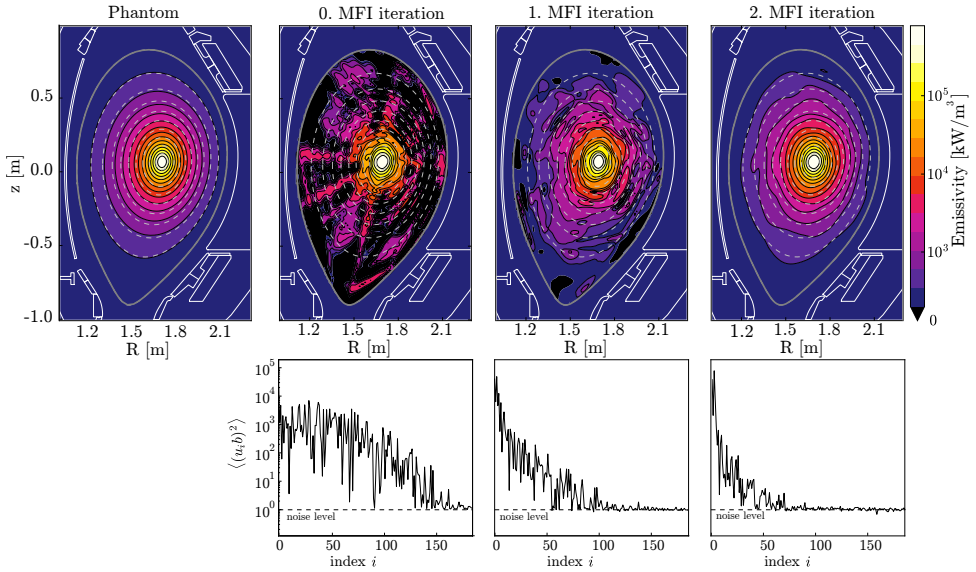


Figure 4. A tomographic reconstruction of the peaked radiation profile is illustrating the effect of the anisotropic MFI iterations on the reconstruction quality. In the upper row is shown phantom profile and the reconstruction for 0-th to 2-th MFI iteration in a nonlinear colorscale. In the lower row is the corresponding energy spectrum $(\mathbf{U}^T\mathbf{b})_i^2$.

Table I. The performance of different regularization selecting methods on the peaked radiation phantom shown in Fig. 4 during MFI iterations. Relative 5% noise was added in the measurements. The value of *optimum* regularization was determined as the position of the minimum between reconstruction and the phantom. Regularization level is described by $q_\lambda$ defined as quantil of set $\{D_i^2\}$ equal to $\lambda$.

| | 0. step | | 1. step | | 2. step | |
|---|---|---|---|---|---|---|
| Method | $q_\lambda(\%)$ | $\delta(\%)$ | $q_\lambda(\%)$ | $\delta(\%)$ | $q_\lambda(\%)$ | $\delta(\%)$ |
| *optimum* | 4 | (12) | 15 | (8) | 37 | (7) |
| GCV | 13 | 13 | 37 | 10 | 56 | **8** |
| PRESS | 28 | 21 | 38 | 10 | 52 | **8** |
| DP | 22 | 18 | 54 | 14 | 76 | 12 |
| $AIC_C$ | 12 | 22 | 56 | 14 | 71 | 11 |

a resolution of 100×150. The noise level, based on the real discharge noise, was in average equal to 2 % of the signal in each channel.

The performance of the method is summarized in Tab. II. The differences between the methods are not significant, and the selected regularization is always close to the optimal value. Nevertheless, DP and $AIC_C$ often provide slightly over-smoothed solutions with a higher residuum. The diversity of the methods on the real data is substantially larger as will be shown in Sec. VI C.

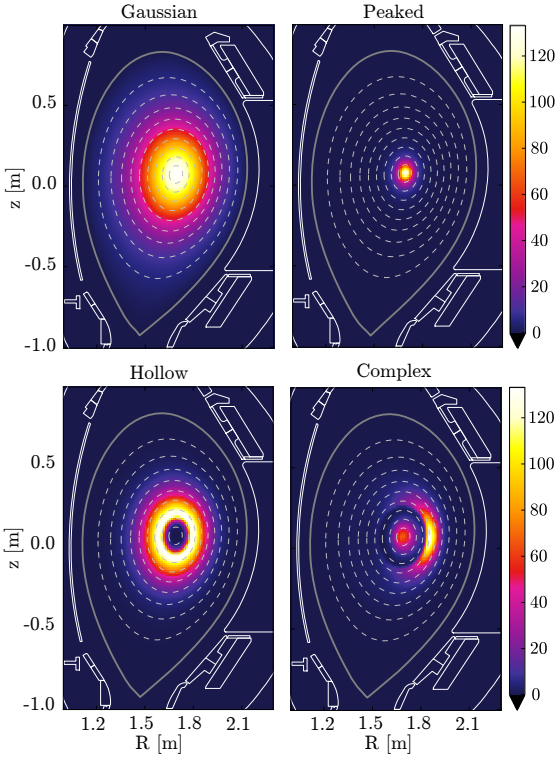


Figure 5. Four phantoms used to evaluate the properties of the regularization selection methods.

## VI. RECONSTRUCTION UNCERTAINTY

A common question related to the tomography is how to estimate the uncertainty of the reconstruction and the derived quantities. The answer is aggravated by the significant contribution of the regularization bias. The contribution of the bias and variance to the relative mean square error (MSE) of the phantom profile is shown in Fig. 6. And obviously, the bias can represent the ma-

Table II. Performance comparisom of different regularization methods on various artificial SXR profiles. The score was measured as a relative deviation [%] with respect to the phantom (Eq. (17)). The first line corresponds to the *ideal* choice of regularization parameters that minimize the difference from phantom.

| | Gaussian | Peaked | Hollow | Complex |
|---|---|---|---|---|
| Method | | $\delta$ (%) | | |
| *optimum* | (1.3) | (3.6) | (6.2) | (6.7) |
| GCV | 1.4 | 3.8 | **7.1** | **8.1** |
| PRESS | 1.9 | **3.7** | 8.2 | 9.0 |
| DP | **1.3** | 5.9 | 9.7 | 9.5 |
| $AIC_C$ | **1.3** | 4.9 | 9.4 | 9.5 |

jority of the MSE. In this section, the components of MSE will be examined, and an analytical formula for the covariance matrix of the solution will be proposed. Additionally, we will describe a way of how to treat the systematical errors.

### A. Statistical and regularization error

The regularized solution of Eq.(5) yields to the following expression for the mean square error (MSE) in $\mathbf{g}_\lambda$:

$$\left\langle (\mathbf{g}_\lambda - \mathbf{g}^*)^2 \right\rangle_k = \sum_{i=1}^{r} f_{i,\lambda}^2 \frac{\mathbf{V}_{ki}^2}{D_i^2} + \tag{18}$$

$$+ \left( \sum_{i=1}^{m} (1 - f_{i,\lambda}) \frac{\mathbf{U}_i^T \mathbf{b}^*}{D_i} \mathbf{V}_{ki} + \left( \left( \mathbf{I}_n - \mathbf{V}\mathbf{V}^T \right) \mathbf{g}^* \right)_k \right)^2$$

where $\langle \cdot \rangle$ indicates averaging over the fluctuating part, $\mathbf{g}^*$ is the accurate but unknown radiation profile and $\mathbf{b}^* = \mathbf{K}\mathbf{g}^*$ is the accurate measurement, unknown as well. The first term on the right is describing the variance caused by statistical uncertainty in the data. The error distribution is assumed to have zero mean and standard deviation of one. The term in the brackets represents the bias of our solution. The left term is the *regularization error* caused by suppressing small features in the measurement $\mathbf{b}^*$. Finally, the last term is a consequence of the rank deficiency of the projection matrix $\mathbf{T}$ and we will call it *singularity error*. Althought the regularization error and the singularity error cannot be estimated without knowledge of the real radiation profile $\mathbf{g}^*$ and the brighness $\mathbf{b}^*$, we can perform a test on a class of the expected radiation profiles to estimate the influence of the bias on the reconstructed quantities. When only a weak regularization is applied, all filtering factors $f_i$ will be close to one and the statistical error will dominate the overall error. On the other hand, if strong regularization is used, most of the $f_i$ values vanish, and the error is dominated by the regularization error. The singularity error can be reduced only by including a priori knowledge more consistent with the solution (like anisotropic smoothing) and by a better angular and spatial coverage of the projection space (cf. Fig. 2).

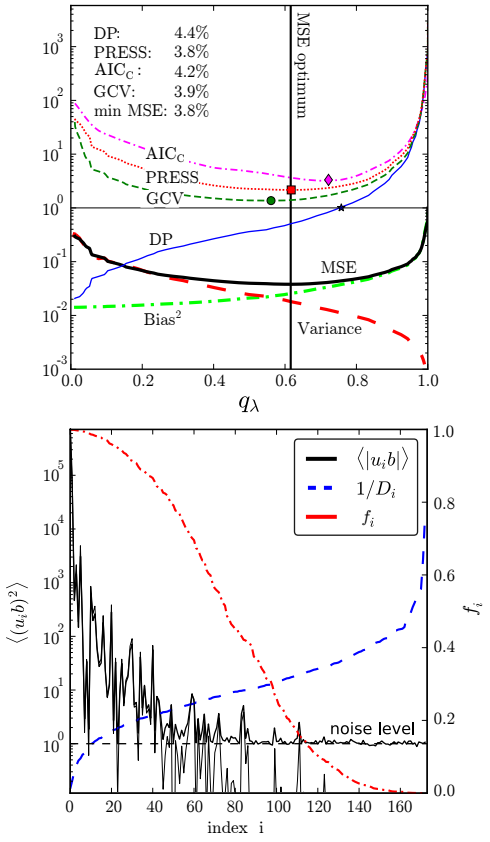


Figure 6. (*top*) Value of the GCV, PRESS, $AIC_C$ and DP are plotted as a function of the regularization level $q_\lambda$. The minima of these functions and the root for DP are indicated by colored markers. The relative MSE obtained by comparison with the phantom and reconstruction is shown by the black thick line. Two components of MSE - the variance and bias are then indicated by a red dashed and green dash-dotted line. The vertical black line indicates position of the MSE minima. (*bottom*) The second figure shows the mean energy spectrum $\langle (\mathbf{U}_i \mathbf{b})^2 \rangle$ of the measured data averaged over time (black thick line) and spectrum of noiseless data (black thin line). The GCV optimal filter factors $f_i = (1 + \lambda/D_i^2)^{-1}$ are plotted in red and blue dashed indicates the unfolding amplification factor $1/D_i$.

The resolution of our reconstruction was assumed to be high enough to keep the pixel discretization error negligible. Moreover, the systematic errors in the geometry of LOSs, their calibration and other imperfection in the model were not included, because they can be significantly reduced as it will be shown in Sec. VIB. And finally, the regularization parameter $\lambda$ is subject to the statistical uncertainty as well. Nevertheless, close to the optimal regularization level, i.e the value of $\lambda$ minimizing MSE (see Fig. 6), the total MSE is only weakly sensitive to the perturbations in $\lambda$.

The statistical uncertainty in the reconstructed profile can be assumed as a lower boundary for the real un-

certainty. Based on the standard uncertainty propagation approach, the covariance matrix of the solution $\mathbf{g}_\lambda$ is given by

$$\Sigma^g_{ij} = \langle (g_i - \langle g_i \rangle)(g_j - \langle g_j \rangle) \rangle = \sum_{k=1}^{r} f_k^2 \frac{V_{ik} V_{jk}}{D_k^2}. \qquad (19)$$

where $\mathbf{V}$ and $\mathbf{D}$ are matrices introduced in the sSVD and sQR methods. Our tests of the phantom reconstructions indicate that the statistical variance is usually about half of the total MSE. Fig. 7a shows a reconstruction of an artifical profile zoomed in the plasma core region. The variances $\Sigma^g_{ii}$ associated with each pixel $i$ can be imaged as it is demonstrated in Fig. 7b. Further, Fig. 7c shows the correlation of a single pixel indicated by the black cross with the neighbor pixels determined from the corresponding row of the covariance matrix. Width and shape of the correlation peak can provide an estimate of the local spatial resolution.

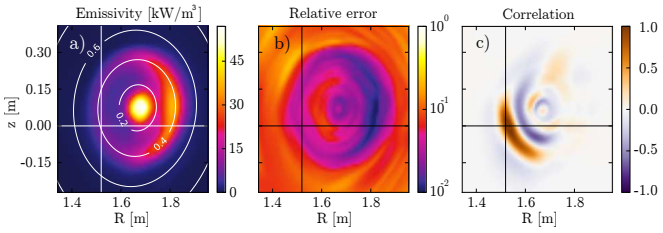


Figure 7. a) A core region SXR emissivity reconstructed from a phantom by the MFI method with anisotropic smoothing and GCV. The white contours are indicating a normalized poloidal flux. b) relative standard deviation $\delta_i = \sqrt{\langle g_i^2 - \langle g_i \rangle^2 \rangle}/\langle g_i \rangle$ of the reconstruction estimated from the diagonal of the covariance matrix $\sqrt{\Sigma_{ii}}/g_i$, c) correlation of the pixel $j$ indicated by the black cross with the surrounding pixels determined from the i-*th* row of the covariance matrix $\Sigma_{ji}/\Sigma_{jj}$. The same pixel $j$ is also marked in (a) and (b) of the figure.

## B. Systematic errors

The unavoidable limitation of the experimentally achievable accuracy is given by the systematical uncertainties in the geometry and calibration of the SXR cameras. Small deviations of the diodes position with respect to the camera slit in combination with a short focal length have a strong influence on the LOS positions and their etendue. The deviation of a diode position of mere 0.2 mm leads to roughly 2 cm shift of LOS in the plasma core and consequently up to 20 % discrepancies of the measured brightness in the regions of the steep SXR radiation, as is observed in typical AUG discharges.

The position and calibration errors are often diagnosed within the multi-camera SXR systems[9,10,55,56] because a large number of viewing angles provides sufficient redundancy of the measurements and the discrepancies can be identified and corrected.

### 1. Relative cross-calibration of the sensitivity

The cross-calibration of the SXR cameras at AUG was evaluated for every discharge in an iterative manner. At first, the initial calibration factors were used to perform a reconstruction of the whole discharge. Afterward, a single correction factor for each camera was obtained in the least squares sense from the reconstructed tomogram. This procedure was repeated until convergence, usually achieved in the first step. Tests on the artificial profiles indicate that the cross-calibration can provide estimates with accuracy well below 0.1 %. The evolution of the estimated cross-calibration factors for five experimental campaigns is shown in Fig. 8. Variation of the core heads is rather low, about 1-2 % within a single campaign. Higher variations as observed in J3 and K1 during the first examined campaign is probably caused by a deviating Be thickness of the filters, which was retrospectively measured to be up to 20 $\mu$m from the designed thickness of 75 $\mu$m. The higher scatters found in the side heads (shown green in Fig. 8) is caused by a low signal level, residual errors in the positioning of these cameras and uncertainties in the sensitivity and etendue of the off-axis channels. Neutron degradation[57] can also be present since the total fluency over the AUG campaign is about $5 \cdot 10^{16}$ neutrons/m$^2$, but no signatures of the neutron damage in the relative calibration were observed.

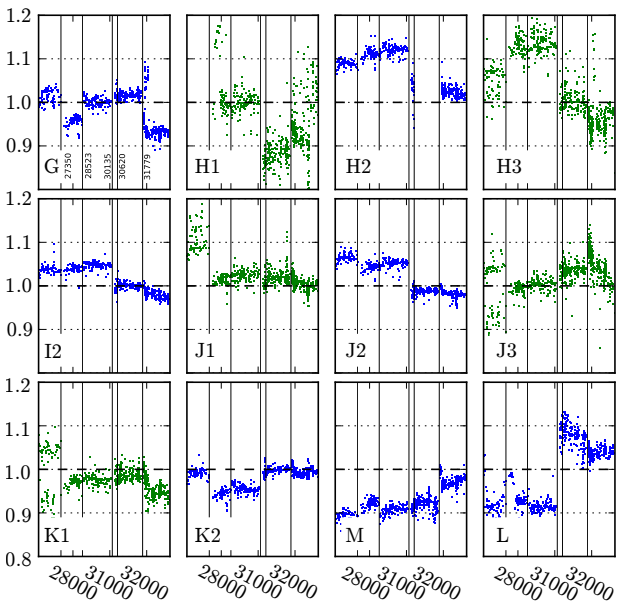


Figure 8. Relative calibration factors for each of 12 regularly used SXR camera heads evaluated for 758 discharges between years 2011 and 2016. The blue points indicate core heads, while the green correspond to the side heads. Vertical lines indicate the opening of the chamber, replacing of the diodes arrays or Be filters and increasing of the viewing angles for cameras G, L and M.

### 2. Adjustments of the viewing geometry

The self-consistent calibration of the heads positions was performed on a set of discharges with negligible centrifugal asymmetries and significant variation in the peaking of the radiation profile. The shape of the magnetic flux surfaces was verified by a comparison between the CLISTE code[58] and the TRANSP equilibrium solver[59] constrained by the kinetic profiles. The deviation in the position of the flux-surfaces in the selected discharges was lower than 5 mm. The optimal position correction was searched by a gradient descent algorithm iteratively modifying the poloidal tilt for each of the 13 heads, to minimize the residuum between the measured brightness and the back-projection. New cross-calibration factors matching the actual geometry had to be estimated in every step. The regularization level had to be fixed to reduce the number of the nested optimization loops and increase the stability. Additionally, since no poloidal asymmetries were expected in the selected discharges, the solution was kept constant on the flux surfaces by the projection matrix $\mathbf{P}$ introduced in the section III B. In the end, the optimal tilt was estimated as a median over the set of tested discharges. The variation in the tilt corrections was about $0°3'$ for the core heads and $0°12'$ for the side heads. The estimated tilts corrections from campaign 2015 are specified in the following table:

| Camera | F | G | H1 | H2 | H3 | I2 | |
|---|---|---|---|---|---|---|---|
| Tilt [°] | -0.26 | -0.99 | -0.68 | -0.46 | 0.10 | -0.82 | |
| Camera | J1 | J2 | J3 | K1 | K2 | L | M |
| Tilt [°] | -1.43 | -1.28 | 1.12 | -1.59 | -0.32 | 1.67 | 1.23 |

No significant changes in these correction factors were observed during the campaign. However, manipulation with the cameras during the tokamak chamber openings has often resulted in small position deviations. Proper cross-calibration and self-consistent positioning of the camera heads has reduced the reconstruction residuums by an order of magnitude. Further, the suppression of the systematic errors has significantly enhanced stability and reliability of all regularization selection methods when used on the experimental measurements. Moreover, the measurements accuracy of the small stationary poloidal asymmetries in the SXR radiation was also significantly improved.

### C. Robustness of the regularization methods for real datasets

The crucial criterion for the choice of the optimal regularization method is their reliability and robustness for the real measurements. All regularization methods have shown an excellent performance on the artificial profiles; the failure rate was zero, and the estimated regularization had never been far from the optimal value minimizing MSE. However, the real data present additional challenges. We have performed a test on 100 randomly chosen discharges representing together 130 000 timepoints. In contrast to the phantom based tests the original emissivity, called also *ground truth*, is unknown. Therefore, our investigation aims to identify the number of over- or under-regularized tomograms. The comparison between regularization methods is presented in Tab. III. The most robust is the PRESS method, working in 99.85 % of the analyzed time-points. Since the GCV is less conservative, the regularization level is usually lower, which lead to a higher number of under-regularized time-points. Most of the failures have occurred in time-points with a low signal-noise ratio (SNR), while a performance similar to the PRESS method was observed in the hotter plasmas, which are usually considered for the SXR tomographic reconstruction. Finally, the DC and $\mathrm{AIC_C}$ methods are providing a comparable level of regularization that is even higher than the estimate from PRESS. The advantage of $\mathrm{AIC_C}$ is higher stability and lower predisposition for extreme values of the regularization parameter than DC. However, both these methods are still limited by considerable uncertainty in the estimation of the real level of the data noise.

Table III. The results of the stability test performed with the regularization methods on the real discharges. The first two columns contain fraction of over- and under-regularized frames and the last column is an average difference of regularization level $q_\lambda$ with respect to the PRESS method.

| Method | over-fitted | over-smoothed | $\langle \Delta q_\lambda \rangle$ |
|---|---|---|---|
| GCV | 6% | 0.1% | -15% |
| PRESS | **0.1**% | **0.05**% | —% |
| DC | 3% | 19% | 13% |
| $\mathrm{AIC_C}$ | 0.4% | 10% | 13% |

## VII. POLOIDAL ASYMMETRIES OF THE SXR RADIATION

The purpose of this section is not to provide an extensive overview of all poloidal asymmetries observed at AUG or introduce new physics; the aim is to demonstrate the capabilities of the new tomograhic procedures introduced at ASDEX Upgrade. Recent studies of the poloidal asymmetries accomplished at the Alcator C-Mod tokamak (see Refs. 60 and 61) motivated an increased interest in the measurements of the impurity distribution on the flux surfaces. Well understood physics and adequately accurate measurements provide valuable information about the fast particle distribution, plasma composition and the plasma position because all these quantities have a strong impact on the observed asymmetry.

The stationary poloidal asymmetry can be characterized by the first angular Fourier components of the stationary emissivity on the magnetic flux surface

$$g(\rho,\theta) = a_0(\rho)\,(1 + a_c(\rho)\cos(\theta) + a_s(\rho)\sin(\theta) + \ldots)\,,$$

where $\rho$ and $\theta$ represent a radial coordinate and a geometrical poloidal angle, $a_c$ will be referred as *in-out* and $a_s$ as *up-down* asymmetry. In-out asymmetries in the poloidal distribution of high-Z impurities are commonly produced by the centrifugal force[62], and in special cases also by fast particles with highly anisotropic distribution function[60]. The neoclassical friction force[61] is expected to be responsible for the up-down asymmetry.

The capabilities of the developed tomographic procedure will be demonstrated on plasma discharge #30812 at 4.40 and 4.65 s. These two cases were selected for the analysis because of a significant variation in the poloidal asymmetry caused by the centrifugal force in the first timepoint and by the trapped minority ions produced by the ion cyclotron range of frequencies (ICRF) heating in the second case. Additionally, both cases were selected shortly before a sawtooth crash when the peaking of the kinetic profiles and of the W density are maximal.

In the first case, the deuteriom plasma was heated only by 2.5 MW of neutral beam injection (NBI) and the core ion temperature reached $T_i = 4.5$ keV, the electron temperature was $T_e = 2.5$ keV at a low core electron density of $3 \cdot 10^{19}$ m$^{-3}$ and the deuterium Mach number (defined as $M_D = \sqrt{m_D v_\phi^2/(2k_B T_i)}$) in the plasma core was equal to 0.33. In the second case, additional 4.3 MW of ICRF power was introduced with an outboard side resonance at $\rho_\theta = 0.4$. The ion and electron temperature was increased to $T_i = 6.0$ keV and $T_e = 4.1$ keV, still at a rather low electron density of $4 \cdot 10^{19}$ m$^{-3}$. The Mach number was equal to 0.21 in the core, causing a nonnegligible centrifugal force. The expected hydrogen minority concentration was roughly 5 % and the effective ionic charge, $Z_{\mathrm{eff}}$, was approximated to 2.0. Since the measured W concentration was of the order of $10^{-3}$, more than 90 % of the core SXR radiation was caused by the tungsten.

The measured SXR brightness of the discharge #30812 at 4.40 s is shown in Fig. 9. For the reconstruction, all available cameras were used except H2 with a broken biasing connector and I1, I3 with different Be filter thickness. The smooth black line with diagonal crosses indicates the back projected brightness from the tomographic reconstruction. Already the shape of the raw data is suggesting a complex peaked-hollow profile with a significant outboard asymmetry. The corresponding tomographic reconstruction evaluated in the resolution 100×150 points is shown in Fig. 10a. The chosen pixel size of 13×13 mm$^2$ is safely below the scale of any features resolvable by the AUG SXR diagnostic. Figure 10b shows a cut through the horizontal midplane of this profile, indicating an evident increase of the outboard SXR emissivity (blue) compared to the inboard emissivity (red). Finally, in Fig. 10c we have evaluated the centrifugal force (CF) asymmetry (red) of the SXR radiation due to W and Bremsstrahlung and compared with the experimental observation (black).

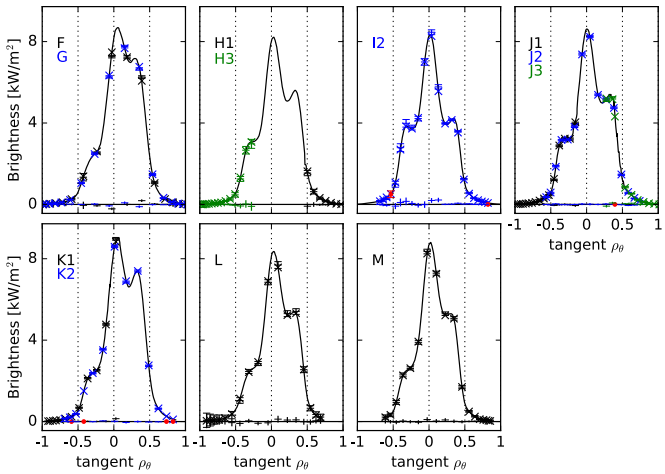


Figure 9. Raw measurements from the discharge #30812@4.4 s (horizontal crosses with errorbars indicating estimated uncertainty), back-calculated values from the tomographic reconstruction (diagonal crosses), cut through projection space in Fig.2 averaged over width of VOS (smooth line), removed points (red dots) and finally crosses close to the zero line are residua between measurements and back-projections. Positive values of the normalized poloidal flux $\rho_\theta$ correspond to the outboard side of the plasma.

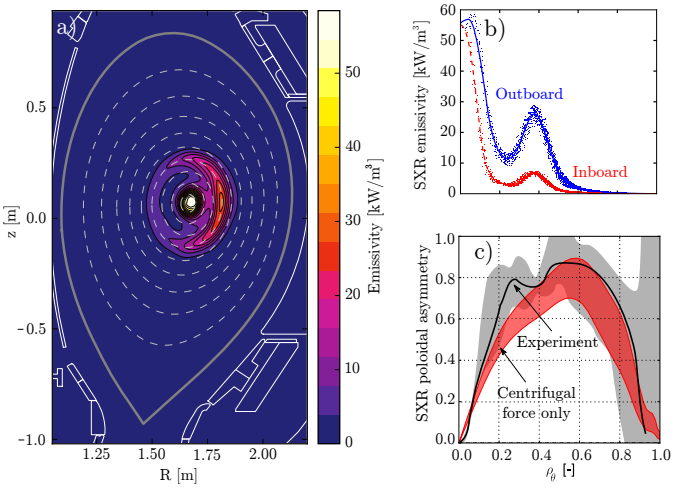


Figure 10. a) Tomographic reconstruction of SXR radiation profile from discharge #30812@4.40 s evaluated in resolution 100×150 pixels with residuum $\chi^2/m = 0.6$ and regularization level $q_\lambda = 55\%$ estimated by GCV b) Emissivity profile through mid-plane, where the full blue line represents the outboard profile and the red dashed line the inboard profile. The scattered points indicate the presence of higher harmonics. c) Experimental asymmetry profile shown by full black line with gray confidence region compared with the calculated CF asymmetry in red.

The confidence interval of the experimental asymmetry profile was estimated from the covariance matrix (Eq. 19) of the reconstruction and assumption of 5 mm uncertainty in the plasma position. The magnetic equilibrium was obtained by the kinetics constrained equilibrium solver in the TRANSP code with the separatrix shape from the CLISTE code. Both profiles match reasonably well, the only larger deviation occurs at $\rho_\theta = 0.25$ corresponding to the valley between the central peak and the outer ring, which is probably caused by the finite radial resolution of the tomography.

The SXR profile before the next sawtooth crash at 4.65 s is very different. Figure 11 shows the experimental data and an elevated level of inboard radiation in cameras F, G, H, L and M is already visible. The tomographic reconstruction is presented in Fig. 12a. The contour image of the emissivity distribution shows an inboard accumulation of W highlighted by a hollow radiation profile. Fig. 12b represents a mid-plane cut through the previous emissivity profile. In this figure an additional outboard asymmetry in the outer regions of the plasma is distinguishable. Finally, in Fig. 12c the experimentally obtained asymmetry is compared with the CF asymmetry, which describes well the outboard region. However, a clear deviation is present around the resonance position of the ICRF, which is caused by the trapped minority ions. However, a detailed analysis and comparison with ICRF models goes beyond the scope of this work and will be addressed in future publications.

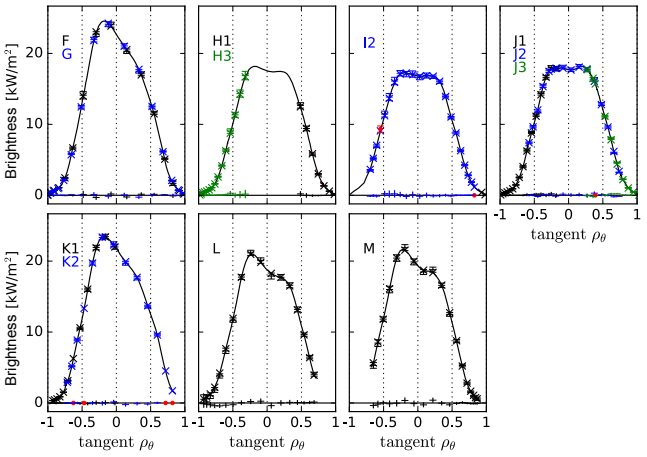


Figure 11. SXR brightness obtained in the discharge #30812@4.65 s during ICRF heating phase. Labeling and color scheme used in these plots is the same as in Fig. 9.

## VIII. CONCLUSIONS

We have introduced a modern multi-head SXR system of the ASDEX Upgrade tokamak. This diagnostic provides excellent coverage of the plasma by 208 lines of sight from 7 different viewing positions. In order to fully take advantage of this diagnostic also for the measurement of the stationary poloidal asymmetries in the SXR radiation, improvements in the precision of the measurement and the reconstruction algorithm were necessary.

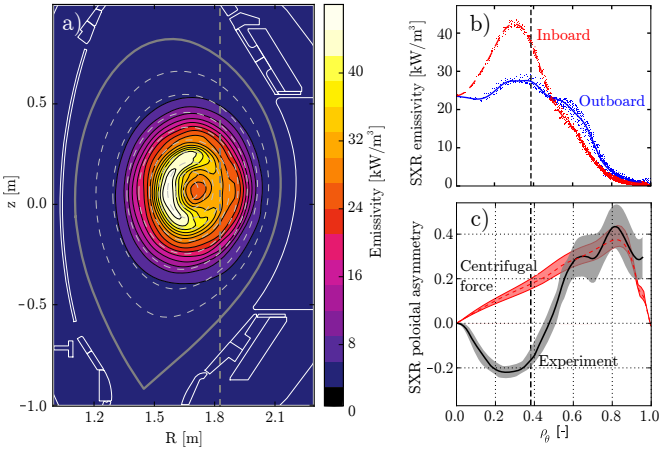


Figure 12. a) Reconstruction of SXR radiation profile from discharge #30812@4.65 s with the residuum $\chi^2/m = 2.4$ and the regularization level $q_\lambda = 49\%$ determined by GCV. The vertical dashed line indicates position of the ICRF resonance. b) Midplane cut through the SXR emissivity profile shows a significant inboard accumulation of W in the core and outboard asymmetry in the outer regions. c) Asymmetry profile obtained from the tomographic reconstruction (black) is compared with the expected centrifugal asymmetry.

We have shown that the small deviations, e.q. in geometry, radiation filters thickness and amplification factors of the SXR diagnostic represent a common limitation of the tomography reconstruction accuracy. Due to the high SXR radiation intensity from tungsten on AUG, the statistical variance is often negligible compared to these systematical errors. We have presented a self-consistent calibration process involving a variation of the diagnostic geometry and a cross-calibration reducing residua between the data and the model by an order of magnitude. Also, the apparent reconstruction artifacts were suppressed, the spatial resolution was enhanced, and the stability of the regularization selecting methods was improved.

To access the full potential of this diagnostic, a new reconstruction algorithm was developed that performs a fast tomographic reconstruction with unprecedented reconstruction quality. The fastest reconstructions were obtained by the improved sparse QR method, followed tightly by the sparse singular value decomposition (sSVD) method. Both algorithms have linear complexity in a number of pixels, but the advantage of the sSVD method is the less complicated algorithm, more suitable for further development.

A critical issue of the Tikhonov regularization is the selection of the regularization parameter. We have compared four methods that are the most suitable for our problem. At first, the performance of these methods

was investigated using artificial profiles where all methods provided an excellent estimate of the regularization parameter. However, tests on real data revealed significant differences. The most stable and reliable was the method based on minimizing of predicted residual error sum of squares (PRESS). Stability of the generalized cross-validation (GCV) is comparable to PRESS only for discharges with high signal to noise ratio (SNR). Occasionally the GCV minimum was not present which has led to significant over-fitting of the low SNR discharges. The unsatisfying performance of discrepancy principle and Akaike information criterion was probably caused by deviations in the estimate of the absolute uncertainty level in the real data. Additionally, we have proposed an analytical formula for the mean square error and the covariance matrix of the reconstruction. The covariance was used to determine the local statistical variance of the reconstruction and also to estimate the local spatial resolution of the tomography.

Finally, the performance of the AUG tomography was demonstrated on the reconstruction of two time slices of a discharge showing large poloidal asymmetries. In the first case, a low-density plasma heated by a neutral beam has possessed a significant centrifugal asymmetry well corresponding to the value calculated from the particle force balance. In the second case, ion cyclotron heating was used on the outer part of the plasma. Close to the resonance position a significant increase of the inboard SXR radiation has occurred. The asymmetry, overcoming the still present centrifugal force, was caused by the trapped fast minority particles with a highly anisotropic temperature distribution. Since there are not many alternative diagnostics measuring highly energetic minority particles at the place of their origin, accurate measurements and a well known physics of the poloidal asymmetries can provide a stringent test of ICRF modeling codes.

## ACKNOWLEDGMENTS

This work has been carried out within the framework of the EUROfusion Consortium and has received funding from the Euratom research and training program 2014–2018 under grant agreement No 633053. The views and opinions expressed herein do not necessarily reflect those of the European Commission.

## REFERENCES

[1] H. Nakamura *et al.*, Fusion Eng. Des. **81**(8), 1339 (2006).
[2] G. Janeschitz *et al.*, J. Nucl. Mater. **290**, 1 (2001).
[3] D. Meade, S. Jardin, *et al.*, in *Proceedings of the 18th IAEA Conf. on Fusion Energy, Sorrento, Italy October* (2000).
[4] T. Pütterich, R. Neu, *et al.*, Nucl. Fusion **50**(2), 025012 (2010).
[5] D. Vezinet, D. Mazon, *et al.*, Fus. Sci and Tech. **63**(1), 9 (2013).
[6] L. Ingesson, B. Alper, *et al.*, Fus. Sci and Tech. **53**(2), 528 (2008).
[7] R. Granetz and P. Smeulders, Nucl. Fusion **28**(3), 457 (1988).
[8] K. Ertl *et al.*, Nucl. Fusion **36**(11), 1477 (1996).
[9] M. Anton *et al.*, Plasma Phys. Cont. Fusion **38**(11), 1849 (1996).
[10] L. Ingesson, B. Alper, *et al.*, Nucl. Fusion **38**(11), 1675 (1998).
[11] T. Odstrcil, T. Pütterich, *et al.*, in *42. EPS P1.133* (2015).
[12] R. Neu, V. Bobkov, *et al.*, Phys. Scripta (T138), 014038 (2009).
[13] M. Sertoli *et al.*, Plasma Phys. Cont. Fus. **53**(3), 035024 (2011).
[14] R. Dux, A. G. Peeters, *et al.*, Nucl. Fusion **39**(11), 1509 (1999).
[15] A. Gude, in *Active Control of Magneto-hydrodynamic Instabilities in Hot Plasmas* (Springer, 2015), pp. 53–104.
[16] D. Mazon, T. Odstrcil, *et al.*, in *25th IAEA FEC* (2014).
[17] V. Igochine, A. Gude, *et al.*, *Hotlink based Soft X-ray Diagnostic on ASDEX Upgrade (IPP 1/338)*, Tech. rep., Max-Planck-Institut für Plasmaphysik (2010), `http://edoc.mpg.de/476537`.
[18] M. Anton, M. Dutch, *et al.*, 22nd EPS **27**(01) (1995).
[19] M. Anton, M. Dutch, *et al.*, RSI **66**(7), 3762 (1995).
[20] A. Ramm and A. Katsevich, *The Radon transform and local tomography* (CRC press, 1996).
[21] M. Weiland *et al.*, Plasma Phys. Cont. Fus. **57**(8), 085002 (2015).
[22] D. Vezinet, V. Igochine, *et al.*, Nucl. Fusion (2016).
[23] A. Tikhonov, in *Soviet Math. Dokl.* (1963), vol. 5, pp. 1035–1038.
[24] N. Iwama *et al.*, in *Image Processing: Theory and Applications* (Elsevier Amsterdam, 1993), pp. 377–380.
[25] A. Wingen *et al.*, J. Comput. Phys. **289**, 83 (2015).
[26] M. Odstrcil, J. Mlynar, *et al.*, Nucl. Instrum. Methods Phys. Res., Sect. A **686**, 156 (2012).
[27] G. Fehmers *et al.*, Inverse problems **14**(4), 893 (1998).
[28] L. Ingesson, *The Mathematics of some Tomography Algorithms used at JET*, Tech. rep., Commission of the European Communities, United Kingdom. JET Joint Undertaking (2000).
[29] N. Terasaki, Y. Hosoda, *et al.*, Fusion Eng. Des. **34**, 801 (1997).
[30] J. Bielecki, L. Giacomelli, *et al.*, RSI **86**(9), 093505 (2015).
[31] P. Hansen, Numerical algorithms **6**(1), 1 (1994).
[32] D. Mazon, D. Vezinet, *et al.*, Nucl. Instrum. Methods Phys. Res., Sect. A **720**, 78 (2013).
[33] J. Mlynar *et al.*, Plasma Phys. Cont. Fusion **45**(2), 169 (2003).
[34] P. Hansen, Inverse problems **8**(6), 849 (1992).
[35] Y. Chen *et al.*, ACM T. Math. Software **35**(3), 22 (2008).
[36] G. Golub *et al.*, *Matrix computations*, vol. 3 (JHU Press, 2012).
[37] Y. Hosoda and T. Torii, Jpn. J. appl. Math. **4**, 287 (1994).
[38] R. Lehoucq, D. Sorensen, *et al.*, *ARPACK users' guide: solution of large-scale eigenvalue problems with implicitly restarted Arnoldi methods*, vol. 6 (Siam, 1998).
[39] C. Van Loan, Numerische Mathematik **46**(4), 479 (1985).
[40] D. Mazon, D. Vezinet, *et al.*, RSI **83**(6), 063505 (2012).
[41] V. Loffelmann, J. Mlynar, *et al.*, Fus. Sci and Tech. **69**(2) (2016).
[42] M. Bertero, C. De Mol, *et al.*, Inverse problems **4**(3), 573 (1988).
[43] P. Hansen, SIAM review **34**(4), 561 (1992).
[44] N. Iwama, H. Yoshida, *et al.*, Appl. Phys. Lett. **54**(6), 502 (1989).
[45] C. Hurvich and C. Tsai, Biometrika **76**(2), 297 (1989).
[46] T. Kitagawa, Jpn. J. appl. Math. **4**(3), 371 (1987).
[47] A. Tikhonov, USSR Comp. Math. Math. Phys. **5**(3), 93 (1965).
[48] D. Girard, SIAM J. Sci. Stat. Comp. **8**(6), 934 (1987).
[49] N. Iwama, *Numerical optimizations of plasma image reconstructions with sparse-data computer tomography*, Tech. rep. (1990).
[50] G. Wahba, SIAM J. Numer. Anal. **14**(4), 651 (1977).
[51] G. Golub, M. Heath, *et al.*, Technometrics **21**(2), 215 (1979).
[52] N. Iwama, T. Tsuji, *et al.*, A bulletin of Daido Technical College **42**, 93 (2006).
[53] H. Akaike, IEEE Trans. Autom. Control **19**(6), 716 (1974).
[54] C. Hurvich *et al.*, J. Roy. Stat. Soc. B **60**(2), 271 (1998).
[55] E. Lyadina, C. Tanzi, *et al.*, EPS, 17C(Part III) (1993).
[56] C. Görner, *Tomographische Untersuchung von globalen Alfvén-Eigenmoden am Stellarator Wendelstein 7-AS*, Ph.D. thesis, Max-Planck-Institut für Plasmaphysic (1998).
[57] R. Korde *et al.*, IEEE Trans. Nucl. Sci. **36**(6), 2169 (1989).
[58] P. McCarthy *et al.*, *The CLISTE interpretive equilibrium code*, Tech. rep., Max-Planck-Institut für Plasmaphysik (1999).
[59] J. DeLucia, S. Jardin, *et al.*, J. Comput. Phys. **37**(2), 183 (1980).
[60] M. Reinke *et al.*, Plasma Phys. Cont. Fus. **54**(4), 045004 (2012).
[61] M. Reinke, J. Rice, *et al.*, Nucl. Fusion **53**(4), 043006 (2013).
[62] J. Wesson, Nucl. Fusion **37**(5), 577 (1997).